

# Numerically Stable Green Function for Modeling and Analysis of Substrate Coupling in Integrated Circuits

Ali M. Niknejad, *Student Member, IEEE*, Ranjit Gharpurey, *Member, IEEE*, and Robert G. Meyer, *Fellow, IEEE*

**Abstract**—The Green function over a multilayer substrate is derived by solving Poisson's equation analytically in the  $z$  coordinate and numerically in the  $x$  and  $y$  coordinates. The  $x$  and  $y$  functional dependence is transformed into a discrete cosine transform (DCT) representation for rapid evaluation. The Green function is further transformed into a numerically stable form appropriate for finite-precision machine evaluation. This Green function is used to solve for the impedance matrix for an arbitrary three-dimensional arrangement of conductors placed anywhere in the substrate. Using this technique, the substrate coupling and loss in IC circuits can be analyzed. A spiral inductor is presented as an example. Experimental measurement results verify the accuracy of the technique.

**Index Terms**—Green function, SPICE models, spiral inductors, substrate coupling, substrate noise.

## I. INTRODUCTION

THE level of integration that can be achieved in high-frequency Si integrated circuits (IC's) is limited by parasitic coupling mechanisms present in Si IC processes. Transistors and other active devices inject current into the substrate through nonlinear capacitors; passive devices and metal traces inject current into the substrate through linear capacitors. The current is transported in the substrate by ohmic and displacement current. The reception mechanism is similar to the injection process. The finite substrate impedance effectively couples every device on an IC to every other device on the chip.

The design of high-speed digital, analog, and, most importantly, mixed-signal circuits requires knowledge of substrate behavior. Knowledge of substrate noise can also help the designer optimize the layout of the circuit. In some cases, knowledge of substrate coupling is absolutely critical. For example, passive devices such as inductors have a quality factor  $Q$  which is limited by substrate loss at high frequencies. Since  $Q$  is an important design parameter for the performance of many circuit topologies, knowledge of substrate loss is integral in the design of high-frequency RF circuits.

In this paper, we will extend a technique of substrate extraction presented in [1]. In the previous work, the sub-

strate parasitics were found by using the boundary-element technique. This involves solving the appropriate electrostatic integral equation using the Green function. This technique used the FFT to speed up the calculation of the Green function. The Green function was derived for a multilayer substrate sitting on a ground plane. However, evaluation of the Green function was limited to the top layer, and this limited the contact locations to the top layer. We will extend this work by deriving a more general Green function. By deriving the Green function over a multilayer substrate and allowing evaluation in any layer, we can place three-dimensional (3-D) contacts anywhere in the substrate, and therefore solve for the impedance matrix for an arbitrary arrangement of contacts. Additionally, we can combine the oxide and passivation layers to our substrate. The oxide layer will support contacts for capacitors, metal traces, and inductors. The substrate layers will support contacts for active devices and substrate contacts. In this way, we can include the current injection from passive and active devices into the substrate coupling calculation.

There are other approaches to the substrate coupling problem. In [2], a finite-difference technique is presented. However, this technique involves discretizing the entire substrate and applying a difference equation at each node. This produces a very large sparse matrix. Sparse matrix techniques can be applied, but matrix sizes are very large regardless of the number of contacts. The integral approach, on the other hand, will produce a matrix size proportional to the number of contacts. Although this produces a much smaller matrix, the resulting matrix is dense and must be inverted using  $O(n^3)$  operations ( $LU$  decomposition or Gaussian elimination). If heuristics are further employed, the resulting matrix may be sparsified [1]. For instance, the FastCap technique [3] uses multipole expansions in free space to accelerate an iterative solver. Similar techniques can be employed here.

## II. THE GREEN FUNCTION APPROACH TO SUBSTRATE EXTRACTION

The boundary-element technique, or method of moments, is well known and widely used [4]. We will only summarize this semianalytical approach for the electrostatic case. We start with Poisson's equation

$$\nabla^2\Phi = -\frac{\rho}{\epsilon} \quad (1)$$

The above equation may be turned into an integral equation of the form

$$\Phi = \int_V \rho(r')G(r, r') d^3r' \quad (2)$$

Manuscript received April 21, 1997; revised December 4, 1997. This material is based on work supported in part by the U.S. Army Research Office under Grant DAAH04-93-F-0200 and in part by Texas Instruments. This paper was recommended by Associate Editor D. Ling.

A. M. Niknejad and R. G. Meyer are with the Department of Electrical Engineering and Computer Sciences and the Electronics Research Laboratory, University of California, Berkeley, CA 94720 USA.

R. Gharpurey is with the Mixed-Signal Design Branch DSP R&D Center, Texas Instruments Inc., Dallas, TX 75265 USA.

Publisher Item Identifier S 0278-0070(98)04123-2.

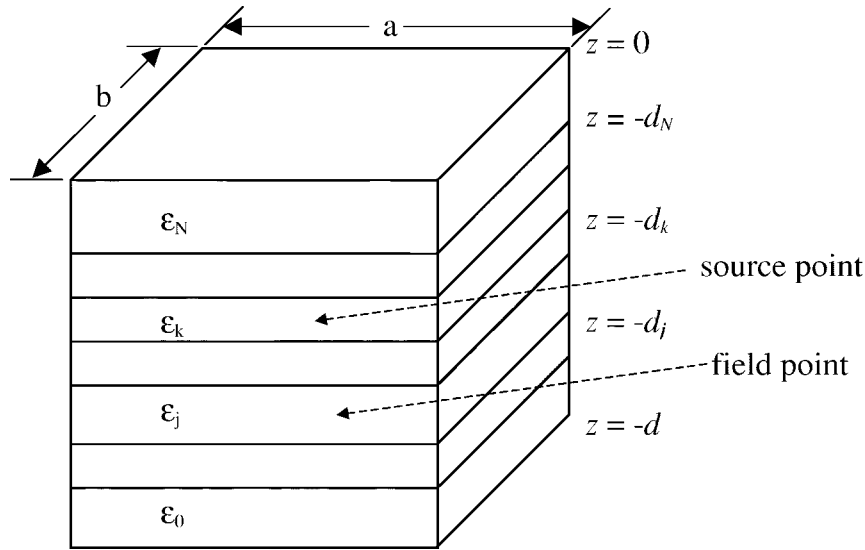


Fig. 1. Geometry of multilayer substrate.

where  $G(r, r')$  is the kernel of the inverse transformation, or the Green function [5]. The Green function can be found by solving the following equation:

$$\nabla^2 G(r, r') = -\frac{\delta(r - r')}{\epsilon}. \quad (3)$$

To find the capacitance of a contact in a medium, one evaluates

$$C = -\epsilon \oint_S E \cdot dS \quad (4)$$

where  $\epsilon$  is the medium permittivity,  $E$  is the electric field in the medium, and  $S$  is the surface area of the contact. To find the resistance of a contact, one evaluates the analogous integral

$$\frac{1}{R} = -\sigma \oint_S E \cdot dS \quad (5)$$

where  $\sigma$  is the material conductivity. Furthermore, if frequency-dependent effects are to be examined, both ohmic and displacement current are present. This can be accounted for by defining a complex conductivity [4]

$$\sigma_c = \sigma + j\omega\epsilon. \quad (6)$$

Equation (2) is an expression for the potential at contact  $i$  due to a charge distribution at contact  $j$ . For sufficiently small contacts  $i$  and  $j$ , we can assume uniform charge distribution, and take the potential of each contact to be the average potential over the volume of the contact. With these approximations, we can rewrite (2) as

$$\bar{\phi}_i = \frac{Q_j}{V_j V_i} \iint_{V_i, V_j} G dV_j dV_i. \quad (7)$$

By considering the above integral for all combinations of contacts, we generate the following matrix equation:

$$[\Phi] = [P][Q]. \quad (8)$$

The matrix  $[P]$  is known as the coefficient-of-potential matrix. By inverting the above relation, we form the coefficient-of-induction matrix, and henceforth we have the desired charge distribution

$$[Q] = [c][\Phi]. \quad (9)$$

It is clear that we must begin by finding the appropriate Green function.

### III. DERIVATION OF THE MULTILAYER GREEN FUNCTION

To derive the electrostatic Green function in a multilayer substrate, consider a point charge placed at  $(x', y', z')$  in layer  $k$  as shown in Fig. 1. The Green function must satisfy Poisson's equation in layer  $j$

$$\nabla^2 G(x, y, z, x', y', z') = \frac{-\delta(x - x')\delta(y - y')\delta(z - z')}{\epsilon_k} \quad (10)$$

where we assume that layer  $k$  has a uniform permittivity of  $\epsilon_k$ . Let  $G = X(x, x')Y(y, y')Z'(z, z')$  in the above equations, thus resulting in

$$Y Z' \frac{d^2 X}{dx^2} + Z' X \frac{d^2 Y}{dy^2} + X Y \frac{d^2 Z'}{dz^2} = -\frac{\delta(x - x')\delta(y - y')\delta(z - z')}{\epsilon_k}. \quad (11)$$

Assume  $X = \cos(m_1 \pi x/a)$  and  $Y = \cos(n_1 \pi y/b)$  in order to satisfy the boundary condition of zero normal  $E$  field on the sidewalls. Making these substitutions results in

$$\begin{aligned} & \sum_{m_1=0}^{\infty} \sum_{n_1=0}^{\infty} \cos\left(\frac{m_1 \pi x}{a}\right) \cos\left(\frac{n_1 \pi y}{b}\right) \\ & \times \left[ \frac{d^2 Z'}{dz^2} - \left( \left(\frac{m_1 \pi}{a}\right)^2 + \left(\frac{n_1 \pi}{b}\right)^2 \right) Z' \right] \\ & = -\frac{\delta(x - x')\delta(y - y')\delta(z - z')}{\epsilon_k}. \end{aligned} \quad (12)$$

By multiplying the above equations by  $\cos(m\pi x/a)$   $\cos(n\pi y/b)$  and by integrating over  $x$  and  $y$  chip dimensions, we get

$$\frac{ab}{4} \left( \frac{d^2 Z'}{dz^2} - \left( \left( \frac{m\pi}{a} \right)^2 + \left( \frac{n\pi}{b} \right)^2 \right) Z' \right) = -\frac{\delta(z-z')}{\epsilon_k} \cos\left(\frac{m\pi x'}{a}\right) \cos\left(\frac{n\pi y'}{b}\right). \quad (13)$$

By defining  $Z'(z, z') = Z(z, z') \cos(m\pi x'/a) \cos(n\pi y'/b)$  and substituting in the above equation, we get a simple second-order differential equation

$$\frac{ab}{4} \left( \frac{d^2 Z}{dz^2} - \gamma_{mn}^2 Z \right) = -\frac{\delta(z-z')}{\epsilon_k} \quad (14)$$

where  $\gamma_{mn} = \sqrt{(m\pi/a)^2 + (n\pi/b)^2}$ . For  $z \neq z'$ , the above equation has the general solution

$$Z = \beta \sinh[\gamma_{mn}(d+z)] + \Gamma \cosh[\gamma_{mn}(d+z)]. \quad (15)$$

Hence, in each layer, the solution must be of the above form. In particular, in layer  $k$ , the solution is of the form

$$Z_k^{u,l} = \left( \beta_k^{u,l} \sinh[\gamma_{mn}(d+z)] + \Gamma_k^{u,l} \cosh[\gamma_{mn}(d+z)] \right) f_k^{u,l}(z') \quad (16a), (16b)$$

where the superscripts  $u$  and  $l$  distinguish between the upper and lower solutions, depending on whether the observation point is above or below the point charge. The potential must be continuous at  $z = z'$ , and the first derivative discontinuity can be found by integrating (14) for  $m, n > 0$ .

$$Z_k^l(z') = Z_k^u(z') \quad (17a)$$

$$\frac{dZ_k}{dz} \Big|_{z'=+\delta} = -\frac{4}{ab\epsilon_k} \frac{dZ_k}{dz} \Big|_{z'=-\delta}. \quad (17b)$$

Using these two conditions, one can solve for the  $z'$  dependence of the potential

$$f_k^{u,l}(z') = \frac{1}{ab\epsilon_k \gamma_{mn} (\Gamma_k^u \beta_k^l - \Gamma_k^l \beta_k^u)} \times 4 \left[ \beta_k^{u,l} \sinh(\gamma_{mn}(d+z')) + \Gamma_k^{u,l} \cosh(\gamma_{mn}(d+z')) \right]. \quad (18a), (18b)$$

In any other layer, the solution takes the same form as (16a) or (16b), depending on whether the observation layer  $j$  is above or below the point charge. Boundary conditions imply that the  $z'$  dependence must be the same as in the layer

$k$ . Hence, the most general solution for the  $z$  dependence of the potential is

$$Z_{j,k}^{u,l} = \frac{4}{ab\epsilon_k \gamma_{mn}} \cosh \vartheta_f \cosh \vartheta_s \times \frac{\left( \beta_j^{u,l} \tanh \vartheta_f + \Gamma_j^{u,l} \right) \left( \beta_k^{l,u} \tanh \vartheta_s + \Gamma_k^{l,u} \right)}{\left( \Gamma_k^u \beta_k^l - \Gamma_k^l \beta_k^u \right)} \quad (19a), (19b)$$

where  $\vartheta_{f,x} = \gamma_{mn}(d - z_{f,s})$ . Here, we introduce the notation of the field point  $z_f = z$  and the source point  $z_s = z'$ . The coefficients  $\beta_k$  and  $\Gamma_k$  still need to be determined. Even though we have two constants, only one is independent. By examining (16), it is clear that either  $\beta_k$  or  $\Gamma_k$  can be factored out and absorbed into the  $z'$  dependence. Due to the boundary condition at  $z = -d$ , i.e., zero potential at the background plane, we must choose  $\beta_0 = 1, \Gamma_0 = 0$ . Furthermore, for each adjacent layer, the following boundary conditions must hold at the interface

$$Z_k \Big|_{z=-d_k} = Z_{k-1} \Big|_{z=-d_k} \quad (20a)$$

$$\epsilon_k \frac{dZ_k}{dz} \Big|_{z=-d_k} = \epsilon_{k-1} \frac{dZ_{k-1}}{dz} \Big|_{z=-d_k}. \quad (20b)$$

The above pair of equations lead to a recursion relation that adjacent layer coefficients must satisfy

$$\begin{pmatrix} \beta_k \\ \Gamma_k \end{pmatrix} = A \begin{pmatrix} \beta_{k-1} \\ \Gamma_{k-1} \end{pmatrix} \quad (21)$$

where we have the matrix  $A$  shown at the bottom of the page.

By employing the above recursion, we can find the coefficients in any layer below the point charge layer  $k$ . Similarly, at the top layer, we impose the boundary condition

$$\frac{dZ_N}{dz} \Big|_{z=-d_{N+1}=0} = 0 \quad (22)$$

This implies that the top layer coefficient values are  $\beta_N = 0, \Gamma_N = -\coth(\gamma_{mn}d)$ . Using the top layer coefficients, and using the inverse of (21), we can recur downward from the top layer to any layer above the point charge layer  $k$ . Hence, all unknowns have been determined. Therefore, for the case of  $m, n > 0$ , we have

$$G_{j,k}^{u,l} = \sum_{m=1}^{\infty} \sum_{n=1}^{\infty} \cosh \vartheta_f \cosh \vartheta_s \cos \frac{m\pi x}{a} \cos \frac{n\pi y}{b} \times \cos \frac{n\pi x'}{a} \cos \frac{n\pi y'}{b} \cdot \frac{4 \left( \beta_j^{u,l} \tanh \vartheta_f + \Gamma_j^{u,l} \right) \left( \beta_k^{l,u} \tanh \vartheta_s + \Gamma_k^{l,u} \right)}{ab\epsilon_k \gamma_{mn} (\Gamma_k^u \beta_k^l - \Gamma_k^l \beta_k^u)}. \quad (23)$$

$$A = \begin{pmatrix} \frac{\epsilon_{k-1}}{\epsilon_k} \cosh^2 \vartheta_k - \sinh^2 \vartheta_k & \left( \frac{\epsilon_{k-1}}{\epsilon_k} - 1 \right) \sinh \vartheta_k \cosh \vartheta_k \\ \left( 1 - \frac{\epsilon_{k-1}}{\epsilon_k} \right) \left( \frac{\epsilon_{k-1}}{\epsilon_k} - 1 \right) \sinh \vartheta_k \cosh \vartheta_k & \cosh^2 \vartheta_k - \frac{\epsilon_{k-1}}{\epsilon_k} \sinh^2 \vartheta_k \end{pmatrix}.$$

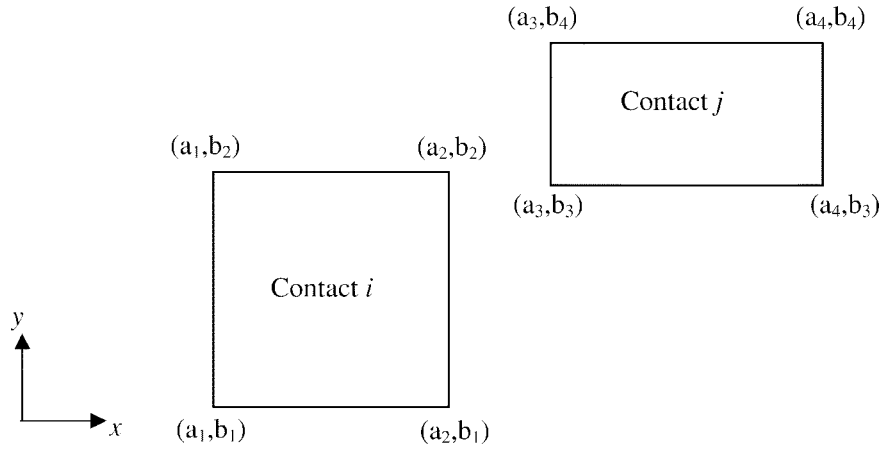


Fig. 2. Contact coordinates.

For the case  $m = 0, n > 0$  or  $n = 0, m > 0$ , the form of (23) remains the same, except that the factor 4 changes to 2 and we have a single summation instead of a double sum. For the case  $m = n = 0$ , the original differential equation (14) has the general solution  $Z_k = B_k z + G_k$ . Applying boundary conditions to adjacent layers results in the following recursion relations:

$$B_j = \frac{\epsilon_j - 1}{\epsilon_j} B_{j-1} \quad (24a)$$

$$G_j = \left( \frac{\epsilon_j - 1}{\epsilon_j} - 1 \right) d_j B_{j-1} + G_{j-1}. \quad (24b)$$

To satisfy boundary conditions at the back plane, we have  $B_0^l = 1, G_0^l = d$ . To satisfy the top-layer boundary condition (22),  $B_N^u = 0 \Rightarrow B_j^u = 0 \forall j \in L_{\text{upper}}$  (upper layers). In addition,  $G_j^u = G^u \forall j \in L_{\text{upper}}$ . By applying the fact that the potential must be continuous across the point charge, and by integrating the differential equation (10), we find

$$Z_{j,k}^{(u)}(z, z') = \frac{B_j^{l,u} \left( \frac{z}{z'} \right) + G_j^{l,u}}{ab\epsilon_k B_k^l}. \quad (25a), (25b)$$

The Green function derived above is represented as a double infinite series which converges slowly. In practical applications, we need a way to evaluate the Green function at many different points in the substrate, thus necessitating a technique for fast evaluation of (23). In [1], a technique for representing (23) as a discrete cosine transform (DCT) is shown. We will use the same technique, and for continuity, we will summarize the work of [1]. We begin by integrating the Green function over the surface of a contact. Equation (4) becomes

$$\bar{\phi}_i = \frac{Q_j}{S_i S_j} \iint_{S_j, S_i} G_{i,j} dS_j dS_i. \quad (26)$$

To find  $p_{i,j} = \bar{\phi}_i / Q_j$ , we integrate (23) and (25) over the surface of contacts  $i$  and  $j$  with coordinates given in Fig. 2.

This results in

$$p_{i,j} = \frac{(B_i^{l,u}\{z, z'\} + G_i^{l,u})}{ab\epsilon_j B_j^l} + \sum_{m=1}^{\infty} \sum_{n=1}^{\infty} k_{mn,ij} C_{mn} \frac{a^2 b^2}{m^2 n^2 \pi^4} \times \frac{\left( \sin\left(m\pi \frac{a_2}{a}\right) - \sin\left(m\pi \frac{a_1}{a}\right) \right)}{(a_2 - a_1)} \cdot \frac{\left( \sin\left(m\pi \frac{a_4}{a}\right) - \sin\left(m\pi \frac{a_3}{a}\right) \right)}{(a_4 - a_3)} \times \frac{\left( \sin\left(m\pi \frac{b_2}{b}\right) - \sin\left(m\pi \frac{b_1}{b}\right) \right)}{(b_2 - b_1)} \cdot \frac{\left( \sin\left(m\pi \frac{b_4}{b}\right) - \sin\left(m\pi \frac{b_3}{b}\right) \right)}{(b_4 - b_3)}. \quad (27)$$

In the above equation,  $C_{00} = 0, C_{m0} = C_{0n} = 2$ , and  $C_{mn} = 4 \forall m, n > 0$ . And

$$k_{mn,ij} = \frac{1}{ab\epsilon_k \gamma_{mn}} \cosh \vartheta_f \cosh \vartheta_s \times \frac{\left( \beta_i^{u,l} \tanh \vartheta_f + \Gamma_i^{u,l} \right) \left( \beta_j^{l,u} \tanh \vartheta_s + \Gamma_j^{l,u} \right)}{\left( \Gamma_j^u \beta_j^l - \Gamma_j^l \beta_j^u \right)} \quad (28)$$

where the subscript  $s$  denotes the source point (with the  $z$  coordinate of the contact in layer  $j$ ), and the subscript  $f$  denotes the field point (with the  $z$  coordinate of the contact in layer  $i$ ).

By using the identity

$$\sin\left(m\pi \frac{a_i}{a}\right) \sin\left(m\pi \frac{a_j}{a}\right) = \frac{1}{2} \left( \cos\left(m\pi \frac{a_i - a_j}{a}\right) - \cos\left(m\pi \frac{a_i + a_j}{a}\right) \right) \quad (29)$$

(27) can be cast into a sum of 64 terms in the form

$$\sum_{m=0}^{\infty} \sum_{n=0}^{\infty} x_{mn} \cos\left(m\pi \frac{a_{1,2} \pm a_{3,4}}{a}\right) \cos\left(n\pi \frac{b_{1,2} \pm b_{3,4}}{b}\right) \quad (30)$$

where

$$x_{mn} = \frac{a^2 b^2}{m^2 n^2 \pi^4} k_{mn} C_{mn}. \quad (31)$$

If we discretize the substrate space in the  $x$ - $y$  directions, and represent the coordinates of the contacts as ratios of integers such that

$$\frac{a_k}{a} = \frac{p_k}{P}; \quad \frac{b_k}{b} = \frac{q_k}{Q} \quad (32)$$

then (30) can be recast as

$$\sum_{m=0}^{P-1} \sum_{n=0}^{Q-1} x_{mn} \cos\left(m\pi \frac{p_{1,2} \pm p_{3,4}}{P}\right) \cos\left(n\pi \frac{q_{1,2} \pm q_{3,4}}{Q}\right). \quad (33)$$

As (33) stands, it cannot be considered a DCT. However, using the following properties of the DCT allows one to compute (30):

$$X_{pq} = \sum_{m=0}^{P-1} \sum_{n=0}^{Q-1} x_{mn} \cos\left(m\pi \frac{p}{P}\right) \cos\left(n\pi \frac{q}{Q}\right) \\ X_{2P-p,q} = X_{p,2Q-q} = X_{2P-p,2Q-q} = X_{p,q}. \quad (34)$$

The Green function can therefore be computed rapidly by employing an FFT to compute the DCT.

The following list summarizes our algorithm for extracting the substrate parasitics.

#### A. For a Given Technology

- 1) Input: Substrate layer data (thickness and dielectric constant and resistivity).
- 2) Input: Metal layer  $z$  coordinates.
- 3) For each pair of metal layers  $i$  and  $j$ , compute the Green function using the DCT method and store results. Due to symmetry of the Green function, for  $N_m$  metal layers, this requires  $N_m(N_m + 1)/2$  DCT's.

#### B. For a Given Layout

- 1) Input: Contact  $x, y, z$  coordinates, width  $w$ , length  $l$ , and thickness  $t$ .
- 2) Form matrix  $[P]$  by accessing DCT of the Green functions.
- 3) Invert  $[P]$  matrix using  $LU$  decomposition.
- 4) Form impedance matrix.

Step A) need only be done once for a given technology. This saves computation time since step A) can be computationally expensive. For three metal layers, six 2-D DCT's need to be performed. Using the FFT, this operation is  $O(p^2 \log p^2)$  where  $p$  represents the accuracy required. For a typical substrate dimension of  $1024 \mu\text{m} \times 1024 \mu\text{m}$ , a  $512 \times 512$  DCT suffices. This sets the minimum metal trace width at  $2 \mu\text{m}$ . Once step A) is performed, step B) uses the precomputed Green functions to build the  $p$  matrix. In other words, the computation time is dominated by  $O(n^3)$  where  $n$  represents the number of contacts, not the DCT size. Although the accuracy of the method depends on the grid size of the DCT, this only affects step A), which is performed once, and not step B), which is performed many times.

## IV. IMPLEMENTATION OF NUMERICALLY STABLE GREEN FUNCTION

Although the derivation of Section III is straightforward, the actual numerical implementation poses many problems. For large values of  $n$  and  $m$ , and deep substrate contacts,  $\tanh \vartheta \rightarrow 1$  and  $\cosh \vartheta \rightarrow \infty$ . Furthermore, for each term  $(\tanh \vartheta + \Gamma/\beta)$ , the ratio  $\Gamma/\beta \rightarrow -1$  so that the numerator factors of (19) approach zero. The denominator of (19) also approaches zero. The product of the ratio and the hyperbolic factors must converge to zero as a whole, due to the physical nature of the solution, but with finite precision, it is very difficult to accurately calculate (19). The above equations, though, may be recast into more numerically stable forms as follows. We begin by rearranging (19a)

$$\left( \frac{(\beta_j^u \tanh \vartheta_f + \Gamma_j^u)}{(\beta_k^u \tanh \vartheta_f + \Gamma_k^u)} \right) \cosh \vartheta_f \cosh \vartheta_s \\ \times \left( \frac{(\beta_k^u \tanh \vartheta_f + \Gamma_k^u)(\beta_k^l \tanh \vartheta_s + \Gamma_k^l)}{\Gamma_k^u \beta_k^l - \Gamma_k^l \beta_k^u} \right). \quad (35)$$

Notice that the we have separated the equations into a factor with only the source layer  $k$  and a factor involving an upper recursion of  $j, k$ . We define  $r_k^l = (\Gamma_k^l/\beta_k^l)$ ,  $\rho_k^u = (\beta_k^u/\Gamma_k^u)$  to simplify notation. We also rewrite (21) as follows:

$$\left( \frac{\beta_k^l}{\Gamma_k^l} \right) = \cosh^2(\vartheta_k) A_k \left( \frac{\beta_{k-1}^l}{\Gamma_{k-1}^l} \right) \quad (36)$$

where

$$A_k = \begin{pmatrix} \frac{\epsilon_{k-1} - \tanh^2 \vartheta_k}{\epsilon_k} & \left( \frac{\epsilon_{k-1} - 1}{\epsilon_k} \right) \tanh \vartheta_k \\ \left( 1 - \frac{\epsilon_{k-1}}{\epsilon_k} \right) \tanh \vartheta_k & 1 - \frac{\epsilon_{k-1}}{\epsilon_k} \tanh^2 \vartheta_k \end{pmatrix} \\ \left( \frac{\beta_k^l}{\Gamma_k^l} \right) = \prod_{p=1}^k \cosh^2(\vartheta_p) A_p \left( \frac{\beta_0^l}{\Gamma_0^l} \right). \quad (37)$$

From the above, we define new coefficients as follows:

$$\left( \frac{\tilde{\beta}_k^l}{\tilde{\Gamma}_k^l} \right) = \prod_{p=1}^k A_p \left( \frac{\tilde{\beta}_0^l}{\tilde{\Gamma}_0^l} \right) \quad (38a)$$

and similarly

$$\left( \frac{\tilde{\beta}_k^u}{\tilde{\Gamma}_k^u} \right) = \prod_{p=k+1}^N A_p^{-1} \left( \frac{\tilde{\beta}_N^u}{\tilde{\Gamma}_N^u} \right). \quad (38b)$$

Using the above definitions, we rewrite (35) as

$$\left( \frac{(\rho_k^u \tanh \vartheta_f + 1)(\tanh \vartheta_s + r_k^l)}{1 - \rho_k^u r_k^l} \right) \\ \times \left( \frac{(\tilde{\beta}_j^u \tanh \vartheta_f + \tilde{\Gamma}_j^u)}{(\tilde{\beta}_k^u \tanh \vartheta_f + \tilde{\Gamma}_k^u)} \right) \frac{\cosh \vartheta_f \cosh \vartheta_s}{\prod_{p=k+1}^j \cosh \vartheta_p}. \quad (39)$$

We will now treat each factor separately. We begin with the first factor in (39). The following recursion relations are

derived from (21):

$$r_k^l = \frac{(1 - q_k) \tanh \vartheta_k + (1 - q_k \tanh^2 \vartheta_k) r_{k-1}^l}{(q_k \tanh^2 \vartheta_k) + (q_k - 1) \tanh \vartheta_k r_{k-1}^l} \quad (40)$$

$$p_k^u = \frac{(p_k - \tanh^2 \vartheta_{k+1}) \rho_{k+1}^u + (p_k - 1) \tanh \vartheta_{k+1}}{(1 - p_k) \tanh \vartheta_{k+1} \rho_{k+1}^u + (1 - p_k \tanh^2 \vartheta_{k+1})} \quad (41)$$

where  $p_k = (\epsilon_{k+1}/\epsilon_k)$ ,  $q_k = (\epsilon_{k-1}/\epsilon_k)$ . Using (40) and (41), and substituting into the first factor of (39) gives<sup>1</sup>

$$\frac{(R_{k-1}^l + q_k \tanh(\vartheta_s - \vartheta_k)) (R_{k+1}^u + p_k \tanh(\vartheta_f - \vartheta_{k+1}))}{q_k R_{k+1}^u - p_k R_{k-1}^l + \tanh(\vartheta_k - \vartheta_{k+1}) (p_k q_k - R_{k+1}^u R_{k-1}^l)} \times \frac{\cosh(\vartheta_s - \vartheta_k) \cosh(\vartheta_f - \vartheta_{k+1})}{\cosh(\vartheta_k - \vartheta_{k+1})} \quad (42)$$

where

$$R_k^l = \frac{\tanh \vartheta_{k+1} + r_k^l}{1 + \tanh \vartheta_{k+1} r_k^l} \quad (43)$$

$$R_k^u = \frac{1 + \rho_k^u \tanh \vartheta_k}{\rho_k^u + \tanh \vartheta_{k+1}}. \quad (44)$$

The above equations satisfy the following recursion relations and terminating conditions:

$$R_k^l = \frac{R_{k-1}^l + q_k \tanh(\vartheta_{k+1} - \vartheta_k)}{R_{k-1}^l \tanh(\vartheta_{k+1} - \vartheta_k) + q_k} \quad (45)$$

$$R_0^l = \tanh \vartheta_1$$

$$R_k^u = \frac{R_{k+1}^u + p_k \tanh(\vartheta_k - \vartheta_{k+1})}{R_{k+1}^u \tanh(\vartheta_k - \vartheta_{k+1}) + p_k} \quad (46)$$

$$R_N^u = \coth(\vartheta_N - \vartheta_{N+1}).$$

Using (45) and (46), (42) can be rewritten as

$$F_k^u = \frac{(R_k^l + \tanh(\vartheta_s - \vartheta_{k+1})) (R_k^u + \tanh(\vartheta_f - \vartheta_k))}{R_k^u - R_k^l + \tanh(\vartheta_k - \vartheta_{k+1}) (R_k^u R_k^l - 1)} \times \frac{\cosh(\vartheta_s - \vartheta_{k+1}) \cosh(\vartheta_f - \vartheta_k)}{\cosh(\vartheta_k - \vartheta_{k+1})}. \quad (47)$$

The above equations may be evaluated in a numerically stable fashion since (43) and (44) are numerically stable as  $\vartheta \rightarrow \infty$ . Equation (47) is valid for field points above the source point charge (upper case). However, due to the symmetry of (39), (47) can be rewritten for the lower case by inspection.

What remains is the second factor in (39). We may calculate this indirectly by using (43) and (44) as well. Rewriting (44) as a ratio

$$R_k^u = \frac{N_k^u}{D_k^u} = \frac{(1 - \tanh \vartheta_k \tanh \vartheta_{k+1})}{(1 - \tanh \vartheta_k \tanh \vartheta_{k+1})} \times \frac{(p_k \tanh(\vartheta_k - \vartheta_{k+1}) D_{k+1} + N_{k+1})}{(\tanh(\vartheta_k - \vartheta_{k+1}) N_{k+1} + p_k D_{k+1})}. \quad (48)$$

The common factor is not canceled for a good reason. When calculating (44) as a ratio, this factor does not play an important role since it always cancels out. But if we wish

to calculate  $N_k^u$  recursively, this factor is important. Let us observe that

$$N_k^u = (1 - \tanh \vartheta_k \tanh \vartheta_{k+1}) \times (p_j \tanh(\vartheta_k - \vartheta_{k+1}) D_{k+1} + N_{k+1}) = \prod_{p=k}^{N-1} (1 - \tanh \vartheta_p \tanh \vartheta_{p+1}) n_k^u. \quad (49)$$

In (49),  $n_k^u$  is the numerator of (43), calculated recursively without the factor of  $(1 - \tanh \vartheta_p \tanh \vartheta_{p+1})$ . By using the above definitions, the first factor in (39) may be rewritten as

$$\frac{\tilde{n}_j^u}{\tilde{n}_k^u} \frac{\cosh(\vartheta_f - \vartheta_{j+1})}{\cosh(\vartheta_f - \vartheta_{k+1})} \frac{\cosh \vartheta_{k+1}}{\cosh \vartheta_{j+1}} \prod_{p=k+1}^j \frac{\cosh \vartheta_p \cosh \vartheta_{p+1}}{\cosh(\vartheta_p - \vartheta_{p+1})} \quad (50a)$$

where  $\tilde{n}_j^u$  is the numerator of (48) modified so that  $\vartheta_j = \vartheta_f$ . A similar analysis for the lower case gives

$$\frac{\tilde{n}_j^l}{\tilde{n}_k^l} \frac{\cosh(\vartheta_f - \vartheta_j)}{\cosh(\vartheta_f - \vartheta_k)} \frac{\cosh \vartheta_k}{\cosh \vartheta_j} \prod_{p=j}^{k-1} \frac{\cosh \vartheta_p \cosh \vartheta_{p+1}}{\cosh(\vartheta_p - \vartheta_{p+1})}. \quad (50b)$$

Utilizing the above results, the complete upper Green function  $z$  dependence can be rewritten as

$$Z_{j,k}^u = \frac{4F_k^u(z_f, z_s)}{abc\epsilon_k \gamma_{mn}} \frac{\tilde{n}_j^u}{\tilde{n}_k^u} \frac{\cosh(\vartheta_f - \vartheta_{j+1})}{\cosh(\vartheta_f - \vartheta_{k+1})} \frac{\cosh \vartheta_k}{\cosh \vartheta_{j+1}} \times \prod_{p=k}^j \frac{\cosh \vartheta_{p+1}}{\cosh \vartheta_p \cosh(\vartheta_p - \vartheta_{p+1})} \times \cosh(\vartheta_s - \vartheta_{k+1}) \cosh(\vartheta_f - \vartheta_k) \quad (51a)$$

and the lower case can be written as

$$Z_{j,k}^l = \frac{4F_k^l(z_f, z_s)}{abc\epsilon_k \gamma_{mn}} \frac{\tilde{n}_j^l}{\tilde{n}_k^l} \frac{\cosh(\vartheta_f - \vartheta_j)}{\cosh(\vartheta_f - \vartheta_k)} \frac{\cosh \vartheta_j}{\cosh \vartheta_{k+1}} \times \prod_{p=j}^k \frac{\cosh \vartheta_{p+1}}{\cosh \vartheta_p \cosh(\vartheta_p - \vartheta_{p+1})} \times \cosh(\vartheta_f - \vartheta_{k+1}) \cosh(\vartheta_s - \vartheta_k). \quad (51b)$$

The above equations are numerically stable, and may be used to implement the algorithm presented in Section III.

## V. EXAMPLES: IC-INTERCONNECT/SPIRAL INDUCTORS

In this section, we illustrate the above described techniques with examples. We start with the simplest possible example of a single metal contact in two hypothetical Si IC processes. The first process, shown in Fig. 3, consists of a thick highly doped substrate and a thin lightly doped epi. The second process, shown in Fig. 4, consists of a thick lightly doped substrate and a thin highly doped epi. The oxide thickness and metal sheet resistivity are the same in both processes. We use a metal contact with a length of 100  $\mu\text{m}$  and a width of 10  $\mu\text{m}$  located at approximately the center of a 256  $\mu\text{m} \times 256 \mu\text{m}$  chip.

Using the algorithm described in Section III, we compute the impedance of the contact. In our case, we subdivided the contact into 100 internal divisions. Fig. 5 is a plot of the magnitude and phase of the contact impedance for the

<sup>1</sup>This follows after much algebra.

$R_{sh}=25m\Omega/sq$	
$\epsilon_{ox} = 3.9$	$t_{ox}=1 \mu m$
$\epsilon_{ox} = 3.9$	$t_{ox}=1 \mu m$
$\rho_{epi} = 100 k\Omega-\mu m$	$t_{epi}=5 \mu m$
$\rho_{sub} = 100 \Omega-\mu m$	$t_{sub}=300 \mu m$

Fig. 3. Lightly doped epi, highly doped substrate.

$R_{sh}=25m\Omega/sq$	
$\epsilon_{ox} = 3.9$	$t_{sub}=1 \mu m$
$\epsilon_{ox} = 3.9$	$t_{ox}=1 \mu m$
$\rho_{epi} = 500 \Omega-\mu m$	$t_{epi}=1 \mu m$
$\rho_{sub} = 100 k\Omega-\mu m$	$t_{sub}=300 \mu m$

Fig. 4. Highly doped epi, lightly doped substrate.

two processes. At increasingly higher frequency, the contact presents a lower impedance due to the capacitive nature of the substrate current injection. The contact has a lower impedance in the first process due to the highly doped bulk substrate layer. On the other hand, the impedance of the second process is very sensitive to the presence of a substrate tap. As shown in Fig. 5, when a  $10 \mu m \times 10 \mu m$  substrate tap<sup>2</sup> is located  $30 \mu m$  away from the contact, the impedance drops to a value below that of process 1. The impedance drops since significant lateral current flows through the surface of the substrate. This indicates the importance of modeling the presence of a substrate tap in such a process. On the other hand, process 1 is not sensitive to the presence of the substrate tap since most current flows vertically through the surface epi layer.

Fig. 6 shows the extracted model, which is highly frequency dependent. We can model the contact impedance with fixed capacitors and a resistor as shown in Fig. 7. This is the physical representation, with a fixed  $C_{MS}$  representing the metal-to-substrate capacitance, and a fixed resistance  $R_{SUB}$  and capacitance  $C_{SUB}$  from the substrate to the ground plane. The values for these physical components can be found over a broad frequency range through optimization. The agreement between the model and the previous simulation result is excellent.

<sup>2</sup>A substrate tap is a metal connection to the surface of the substrate.

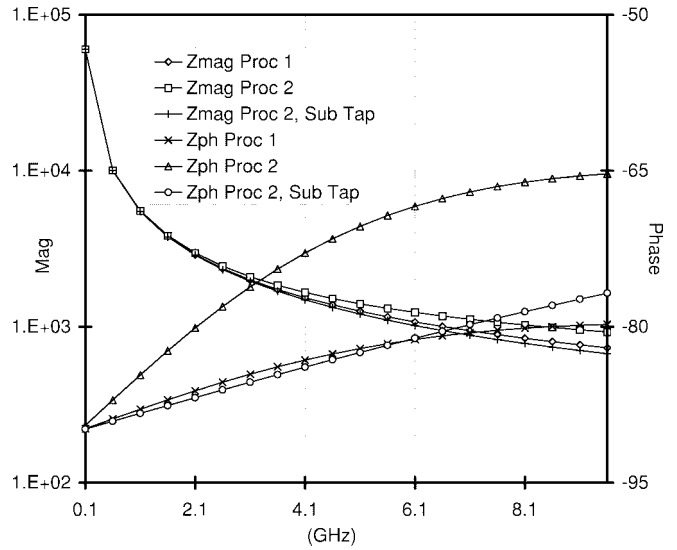


Fig. 5. Magnitude and phase of contact to substrate impedance for processes 1 and 2.

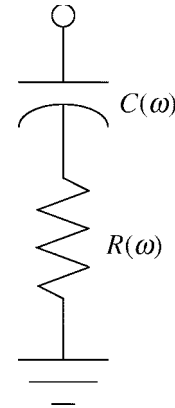


Fig. 6. Frequency-dependent model of contact.

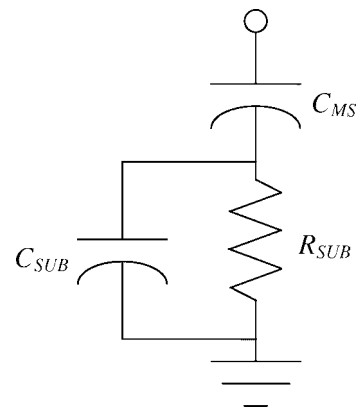


Fig. 7. Frequency-independent model of contact.

Using the same simulation setup as described before, we examine the coupling impedance between two contacts. Two contacts are placed symmetrically around the center of the chip, one contact of length  $100 \mu m$  and width  $10 \mu m$ , the other contact of length  $50 \mu m$  and width  $10 \mu m$ . Three values of spacing are simulated: 2, 5, and  $10 \mu m$ . Similar to the single

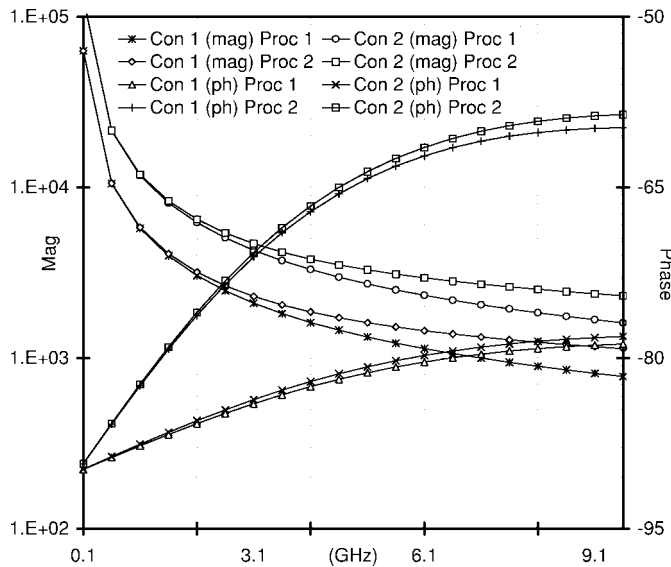


Fig. 8. Contact to substrate impedance for two contacts of different area.

contact case, the contact to substrate impedance is plotted in Fig. 8. For both processes, the larger contact naturally presents a lower impedance. The coupling impedance values are plotted in Figs. 9 and 10. Here, we see significant differences. For the first process, Fig. 9 shows that the value of the spacing is very significant, and the coupling impedance changes by orders of magnitude for different spacing values. For the second process, however, Fig. 10 shows that the contact impedance is not too sensitive to the spacing used. This is understandable since the second process coupling current flows laterally through surface, whereas in the first process, lateral current flows through the bulk substrate. Fig. 10 also shows that the coupling impedance changes dramatically in the presence of a substrate tap placed between the contacts. As a result, a significant fraction of the lateral surface current flows to ground instead of to the other contact. The same isolating effect is not seen in the first process due to the highly resistive surface layer. Similar to before, frequency-independent circuits can be constructed to model the impedance over a wide frequency range.

Next, we consider the more complicated example of a spiral inductor with a geometry shown in Fig. 11. The spiral is  $200 \mu\text{m} \times 200 \mu\text{m}$  on the sides, with a 4.5 turn metal of width  $12.8 \mu\text{m}$  and a line-to-line spacing of  $4 \mu\text{m}$ . Even though its geometry is more complex, it is just a collection of contacts similar to the single and coupled contacts we analyzed.

Spiral inductors have been modeled successfully in GaAs microwave circuits before, but the lossy Si substrate has made the modeling of spirals on Si substrate more difficult. The losses of the Si substrate are substantial, and cause  $Q$ -degradation effects at high frequency. Hence, this analysis gives us the important missing ingredient in analyzing spiral inductors.

We extract the spiral impedance using two different processes shown previously in Figs. 3 and 4. Both substrates are typical of Si IC processes. Again, using the previously described algorithm, we compute the substrate impedance matrix of the structure at the frequencies of interest.

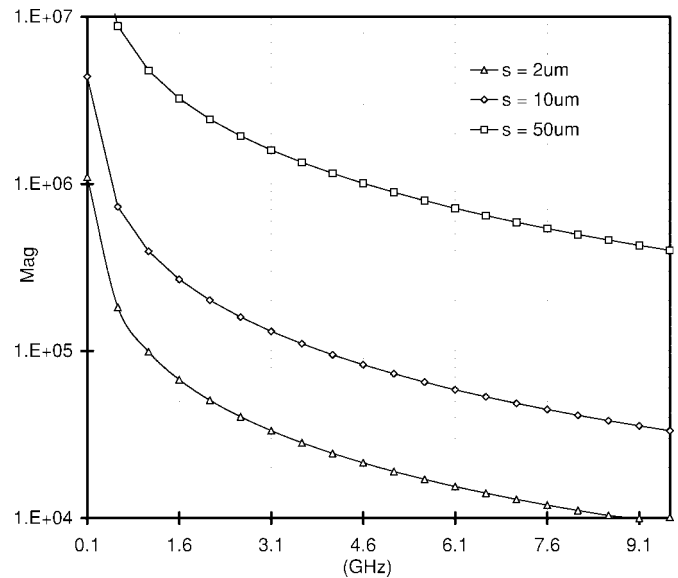


Fig. 9. Substrate coupling impedance for process 1 for different contact spacing values.

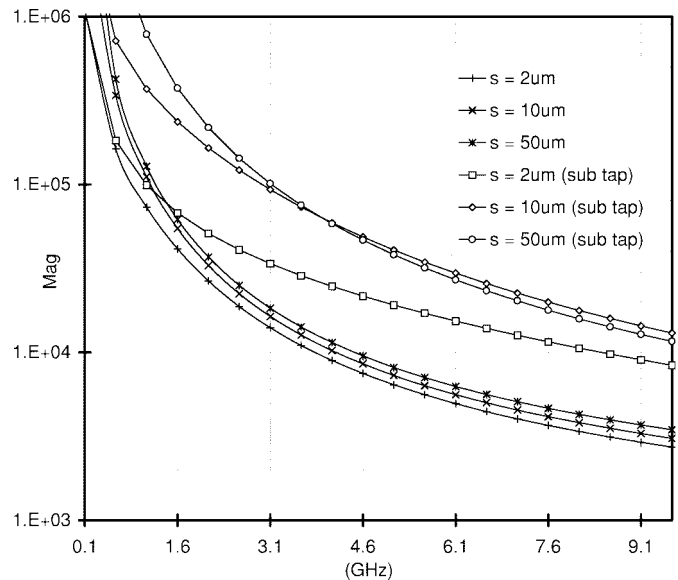


Fig. 10. Substrate coupling impedance for process 2 for different contact spacing values.

To account for magnetic effects in the spiral, we use the well-known geometric mean distance (GMD) approximation [6]–[8]. In this approximation, the substrate is ignored, which assumes that the magnetic effects produced by the substrate are negligible.<sup>3</sup> Hence, we calculate the free-space mutual inductance between every segment and every other segment. The finite thickness of the conductors is accounted for by the GMD approximation.

The resulting equivalent frequency-dependent circuit is used for ac analysis, and  $y$  parameters are computed over a broad frequency range. From the  $y$  parameters, the equivalent  $\pi$  circuit shown in Fig. 12 can be derived. The equivalent ex-

<sup>3</sup>Calculation of the inductance and reflected resistance over a conductive substrate is the subject of another paper.

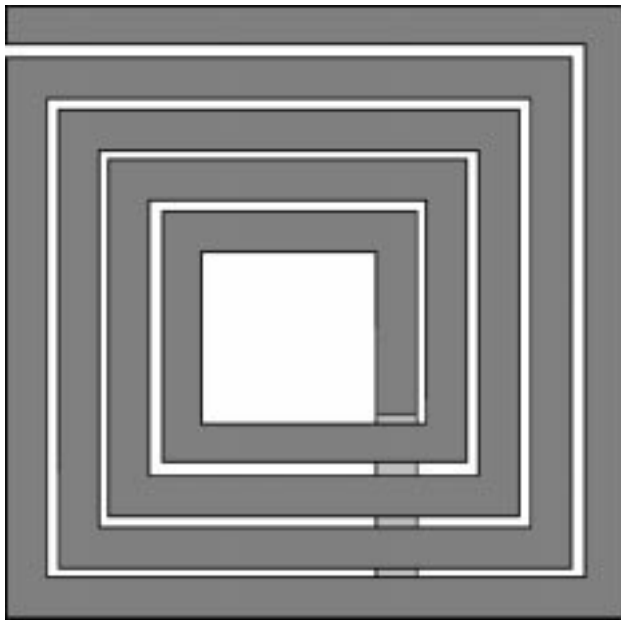


Fig. 11. Square spiral inductor.

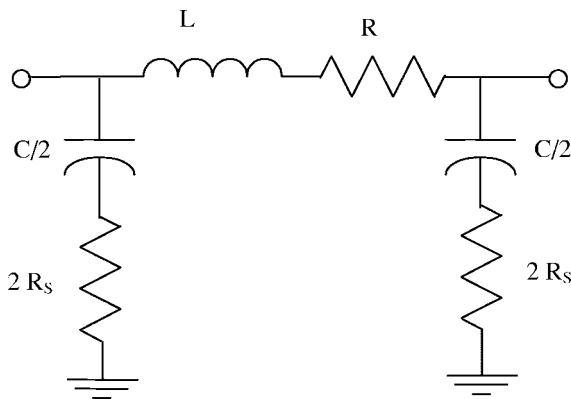


Fig. 12. Narrow-band equivalent circuit of square spiral.

tracted series inductance and resistance are plotted in Fig. 13.<sup>4</sup> It is interesting to note that the effective series inductance and resistance show a drastically different behavior in the two cases shown. For process 2, the effective inductance increases with frequency, whereas in process 1, the effective inductance decreases with frequency. Also, the effective series resistance of process 2 decreases faster than process 1. These effects are due to the different substrate coupling present in both processes. In reality, the process 2 spiral would be near a substrate tap which would isolate the metal segments.

Fig. 14 shows the extracted resistance and capacitance to the substrate. The capacitance and resistance change as a function of frequency since the current transport mechanism changes. At low frequency, the current transport is primarily ohmic, whereas at higher frequencies, displacement current becomes important. Finally, the plot of the quality factor

<sup>4</sup>Notice that negative series resistance is a modeling effect and not a physical effect. The input impedance of the structure has a positive real part at all frequencies. This behavior is observed at frequencies above the self-resonant frequency where the device no longer acts like an inductor, but a capacitor.

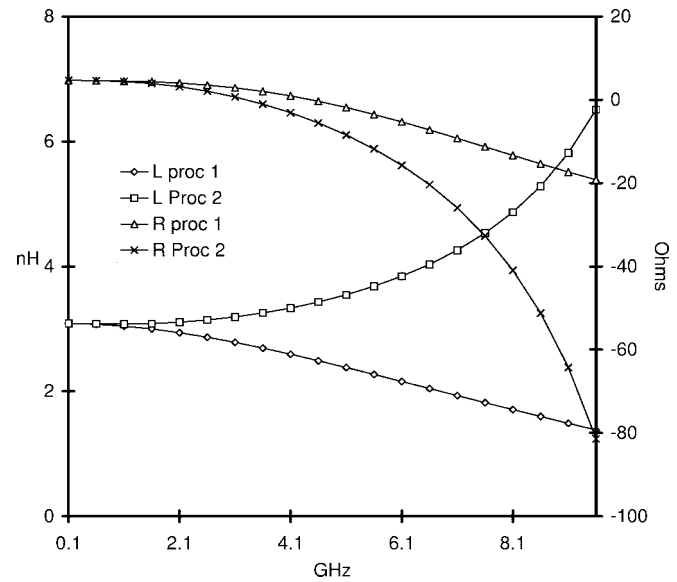


Fig. 13. Extracted series inductance and resistance of square spiral.

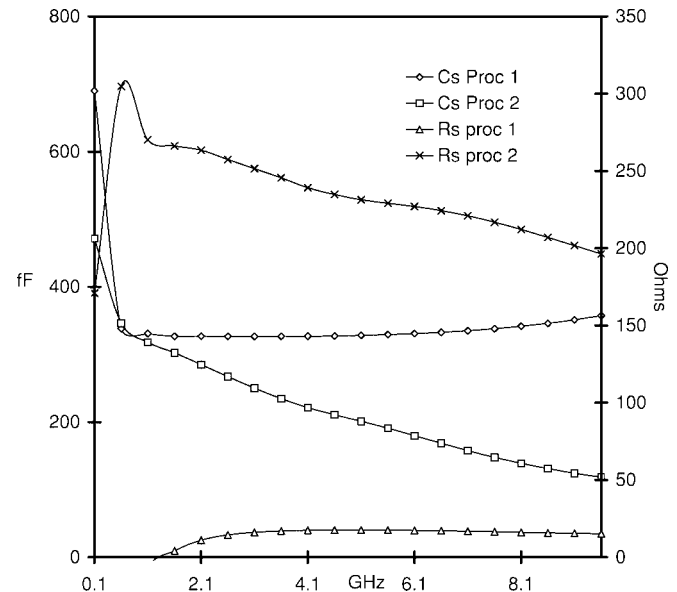


Fig. 14. Extracted shunt substrate capacitance and resistance.

$Q$  for both processes is shown in Fig. 15.<sup>5</sup> Again, the  $Q$  shows different behavior for the different processes due to the substrate impedance difference.

In a manner similar to the single contact, the dynamics of the substrate can be captured in a frequency-independent model as shown in Fig. 16. The equivalent circuit parameters can be derived by averaging the narrow-band parameters over the frequency range of interest, or by optimization.

We have seen that substrate extraction for the spiral inductor is of paramount importance. Due to the low self-resonant frequency of these structures, we often use these inductors close to their self-resonant frequencies. Therefore, it is important to be able to extract frequency-dependent behavior at high frequencies. To model frequency-dependent effects,

<sup>5</sup>Negative  $Q$  occurs beyond the self-resonant frequency of the device where the device acts like a capacitor rather than an inductor.

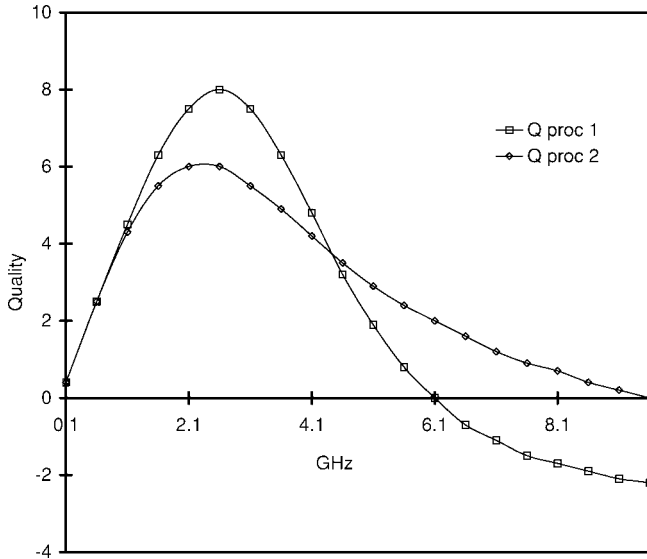


Fig. 15. Quality factor of square spiral inductors.

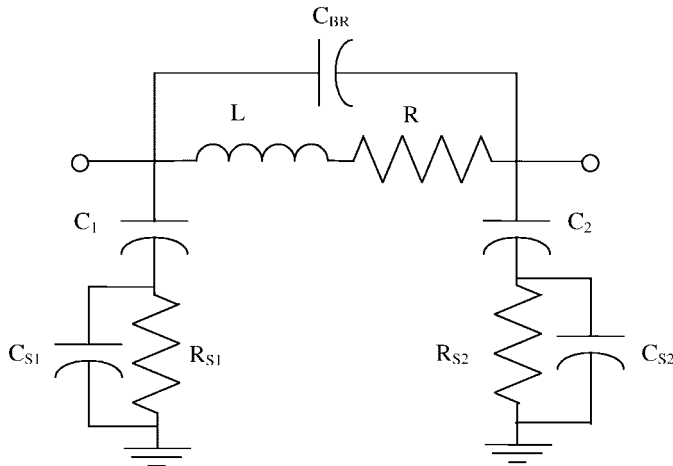


Fig. 16. Broad-band equivalent circuit of square spiral.

the substrate matrix must be calculated and inverted at each frequency of interest.

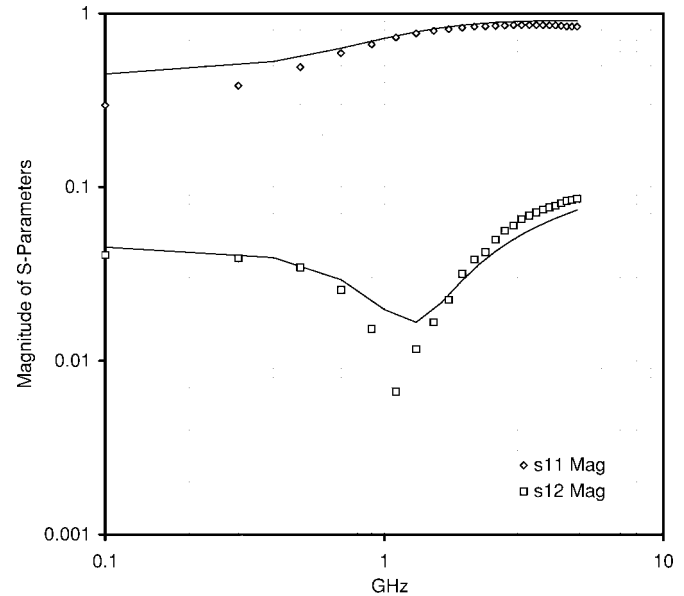
## VI. EXPERIMENTAL VERIFICATION

Several test structures were fabricated in a BiCMOS process and measured in the frequency range of 100 MHz–6 GHz. The agreement between theory and measurement is excellent [9]. To demonstrate this, consider the coupling that occurs between two large metal structures residing on the same substrate. The coupling occurs both through the substrate and through the oxide, a good candidate for our analysis technique. This coupling can be a significant problem. For instance, in any amplification stage, the substrate coupling can act as parasitic feedback, lowering the gain and possibly causing oscillations to occur.

We examine the coupling that occurs between two square spiral inductors separated by a distance of  $100 \mu\text{m}$ . Each square spiral consists of eight-turns of  $7 \mu\text{m}$  wide metal traces with a separation of  $5 \mu\text{m}$  and an inner hole width of  $44 \mu\text{m}$ . Approximate process parameters appear in Table I.

TABLE I  
APPROXIMATE PROCESS PARAMETERS

Metal 2	$R_{\text{sh}} = 33\text{m}\Omega/\text{sq}$	$t = 1.27\mu\text{m}$	$C_{\text{sub}} = 14\text{aF}/\mu\text{m}^2$
Metal 1	$R_{\text{sh}} = 50\text{m}\Omega/\text{sq}$	$t = 1.00\mu\text{m}$	$C_{\text{sub}} = 21\text{aF}/\mu\text{m}^2$
Metal 0	$R_{\text{sh}} = 100\text{m}\Omega/\text{sq}$	$t = 0.40\mu\text{m}$	$C_{\text{sub}} = 105\text{aF}/\mu\text{m}^2$
Buried Layer	$\rho = 0.085\Omega\text{-cm}$	$t = 1\mu\text{m}$	$\text{p}^+\text{Si}$
Bulk Substrate	$\rho = 20\Omega\text{-cm}$	$t = 675\mu\text{m}$	$\text{p}^+\text{Si}$

Fig. 17. Measured and simulated  $s$  parameters of the coupled spirals.

In this configuration, although some coupling also occurs through the magnetic field, the dominant coupling mechanism is electrical in nature. More interestingly, since the devices are inductive in nature and the coupling is capacitive, we can expect some resonance phenomena to occur. The measured and simulated  $s$  parameters of such a device appear in Fig. 17.<sup>6</sup> As can be seen from the figure, the simulation results predict the coupling behavior accurately, such as the minimum  $s_{21}$ . To gain further insights into the coupling, we plot the power isolation from one spiral to the other using the following equations. For an arbitrary two-port driving a load  $R_L$  by a source resistance  $R_S$ , it can be shown that

$$\frac{P_L}{P_{\text{in}}} = \frac{R_L \| G_t \|^2}{\text{Re}[Z_{\text{in}}]} \quad (52)$$

where  $G_t$  is the current gain through the two-port and  $Z_{ib}$  is the impedance looking into the two-port from the source side

$$G_t = \frac{z_{12}}{R_L + z_{12}} \quad (53)$$

$$Z_{\text{in}} = z_{11} - \frac{z_{12}^2}{R_L + z_{22}} \quad (54)$$

Using the above equations, we plot the measured and simulated power isolation for the coupled inductors in Fig. 18, where a  $50 \Omega$  load resistance is used in the above equations. Clearly, there are two frequencies where the isolation is

<sup>6</sup>The inconsistency between the measurement and simulation is believed to be due to errors in the measurement process introduced by the calibration step. See [9] for further information.

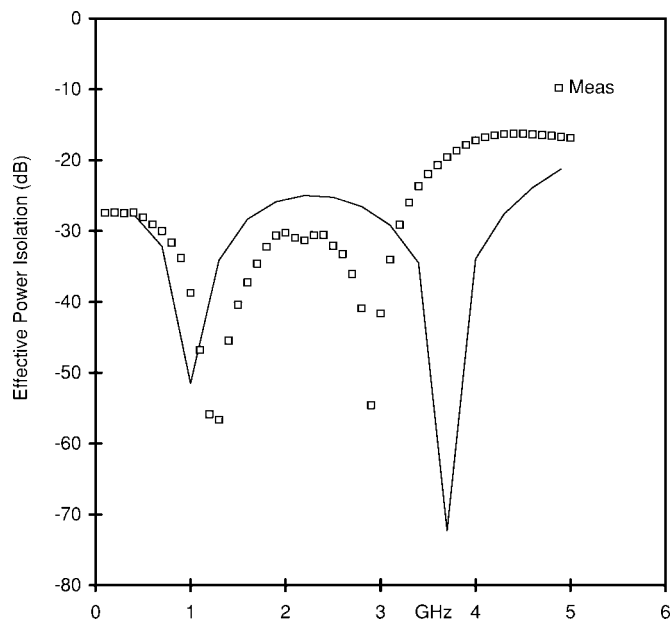


Fig. 18. Measured and simulated isolation between the coupled spirals.

maximum. These frequencies depend on the geometrical layout of the spirals, and this gives the designer the powerful option of placing the spirals in locations to maximize isolation.

VII. CONCLUSION

In this paper, we have discussed a technique for substrate parasitic extraction over a multilayer Si substrate. We derived the appropriate Green function, and we found a numerically stable transformation of the Green function. We also used the DCT to calculate the Green function efficiently. This approach has been applied to spiral inductors, and  $y$  parameters have been calculated over a broad range of frequencies. The results demonstrate the importance of accurate substrate modeling since the desired inductance, resistance,  $Q$  factor, and self-resonant frequency are affected by the substrate. The accuracy of this technique has also been verified experimentally. These predictions, though, must be substantiated by further study since we have neglected other important frequency-dependent effects such as the possibility of skin effect in the bulk substrate. At high frequency, the effective substrate thickness can change, modifying the substrate impedance.

REFERENCES

[1] R. Gharpurey, "Modeling and analysis of substrate coupling in integrated circuits," Ph.D. dissertation, Univ. California, Berkeley.  
 [2] N. K. Verghese, D. J. Allstot, and S. Masui, "Rapid simulations of substrate coupling in mixed-mode IC's," in *Proc. IEEE Custom Integrated Circuits Conf.*, May 1993, pp. 18.3.1–18.3.4.  
 [3] K. Nabors and J. White, "FastCap: A multipole accelerated 3-D capacitance extraction program," *IEEE Trans. Computer-Aided Design*, vol. 10, pp. 1447–1459, Nov. 1991.  
 [4] S. Ramo, J. R. Whinnery, and T. Van Duzer, *Fields and Waves in Communication Electronics*, 3rd ed. New York: Wiley, 1994, pp. 324–330.

[5] G. F. Roach, *Green's Functions*, 2nd ed. New York: Cambridge Univ. Press, 1982.  
 [6] N. M. Nguyen and R. G. Meyer, "Si IC-compatible inductors and LC passive filters," *IEEE J. Solid-State Circuits*, vol. 27, pp. 1028–1031, Aug. 1990.  
 [7] H. M. Greenhouse, "Design of planar rectangular microelectronic inductors," *IEEE Trans. Parts, Hybrids, Packag.*, vol. PHP-10, pp. 101–109, June 1974.  
 [8] F. W. Grover, *Inductance Calculations*. New York: Dover, 1962.  
 [9] A. M. Niknejad and R. G. Meyer, "Analysis, design, and optimization of spiral inductors and transformers for Si RF IC's," submitted for publication.



**Ali M. Niknejad** (S'92) was born in Tehran, Iran, on July 29, 1972. He received the B.S.E.E. degree from the University of California, Los Angeles, in 1994, and the M.S. degree in electrical engineering from the University of California, Berkeley, in 1997, where he is now pursuing the Ph.D. degree.

He has held several internship positions in the electronics industry. In the summer of 1994, he worked at the Hughes Aircraft Advanced Circuit Technology Center (ACTC), Torrance, CA, investigating wide-band current feedback op-amp topologies. During the summer of 1996, he worked at Texas Instruments, Dallas, TX, where he studied substrate coupling. During the summer of 1997, he worked at Lucent Technologies (Bell Labs), Murray Hill, NJ, where he investigated power amplifier topologies for wireless applications. His current research interests include high-frequency electronic circuit design, modeling of passive devices and substrate coupling, digital wireless communication systems, numerical methods in electromagnetics, and RF CAD.



**Ranjit Gharpurey** (S'92–M'95) received the B.Tech. degree from the Indian Institute of Technology, Kharagpur, in 1990, where he was awarded the President of India Gold Medal for the best academic performance in the class of 1990, and the M.S. and Ph.D. degrees from the Department of Electrical Engineering and Computer Sciences, University of California, Berkeley, in 1992 and 1995, respectively.

He is currently with the Circuit Technology Laboratory, DSP R&D Center, Texas Instruments, Dallas, TX. His interests are in the area of RF circuit design and modeling.



**Robert G. Meyer** (S'64–M'68–SM'74–F'81) was born in Melbourne, Australia, on July 21, 1942. He received the B.E., M.Eng.Sci., and Ph.D. degrees in electrical engineering from the University of Melbourne in 1963, 1965, and 1968, respectively.

In 1968, he was employed as an Assistant Lecturer in Electrical Engineering, University of Melbourne. Since September 1968, he has been employed in the Department of Electrical Engineering and Computer Sciences, University of California, Berkeley, where he is now a Professor. His current research interests are high-frequency analog integrated-circuit design and device fabrication. He has acted as a consultant on electronic circuit design for numerous companies in the electronics industry. He is coauthor of the book *Analysis and Design of Analog Integrated Circuits* (Wiley, 1993), and Editor of the book *Integrated Circuit Operational Amplifiers* (IEEE Press, 1978).  
 Dr. Meyer was President of the IEEE Solid-State Circuits Council and was an Associate Editor of the IEEE JOURNAL OF SOLID-STATE CIRCUITS and of the IEEE TRANSACTIONS ON CIRCUITS AND SYSTEMS.